The Eighth Asia-Pacific Conference on Wind Engineering, December 10-14, 2013, Chennai, India

INVESTIGATION ON COHERENCE CHARACTERISTICS OF WIND PRESSURES ON HEMISPHERICAL DOMES

Yuan-Lung Lo[1], Chung-Lin Fu[2], Chia-Kuo Wang[3]

[1]*Assistant Professor, Dept. Civil Eng., Tamkang University, New Taipei City, Taiwan,* yllo@mail.tku.edu.tw

[2]*Research Fellow, WERC, Tamkang University, New Taipei City, Taiwan,* fcl@mail.tku.edu.tw

[3]*Assistant Research Fellow, WERC, Tamkang University, New Taipei City, Taiwan,* c.k.wang@gmail.com

ABSTRACT

Systematic wind tunnel tests were conduct to investigate coherence characteristics of any two fluctuating wind pressures along the meridian on hemispherical domes under smooth and turbulent wind flows. Reynolds number was alternated from 6.6×10^4 to 1.9×10^6 for both flows. Contour plots of root-coherence values with respect to frequency and reference location were given to show only little inconsistency due to Reynolds number effect. On the other hand, approaching turbulence, simulated in turbulent flow, showed distinct differences, especially in the windward and dome apex region. A modified form proposed by Hui et al (2009) was applied for the approximation of root-coherences rather than Davenport's proposed. It was concluded that not only the location of the reference tap but also the distance between two taps, can significantly determine the distribution features of coherences.

Keywords: Hemispherical Dome, Surface Pressure, Coherence

Introduction

Large span roof structures are common designs for various structures in a modern society, such as sport stadiums, coal/oil storage, museums, or certain symbolic, religious structures. Rather than seismic loads, what it may concern in this kind of structures is usually its curved geometry over a large span, which may raise its sensitivity to wind loads. Maher (1965) first conducted measurements of mean wind pressures on hemispherical domes with various height-span ratios. He indicated that the drag force coefficient is less sensitive when Reynolds number is larger than 1.4×10^6. Toy et al (1983) then conducted similar experiments by alternating the approaching turbulences in the test section. Results showed that the increasing turbulence impels the movement of separation and reattachment points along the dome surface. Taylor (1991) continued to indicate that under a turbulent flow, say turbulence intensity 15% or larger, the characteristics of wind pressures remain consistent when Reynolds number is larger than 1.7×10^5, which is an applicable operational value in most of tunnel tests. Ogawa et al (1991) investigated mean and R.M.S. wind pressures and spectrum characteristics of three hemispherical domes in laminar and turbulent flows. He gave the idea that dividing the dome roof surface into three zones: frontier zone, apex and side zone, and wake zone. He also proposed conventional models for approximations of power spectra and cross spectra. Letchford and Sarkar (2000) investigated the effect of surface roughness on the pressure distributions and on the overall drag and lift forces. Uematsu and Tsuruishi (2008) proposed a computer-assisted wind load evaluation system for the design of roof cladding of hemispherical domes based on artificial neural network theory. The statistics of mean, R.M.S., skewness and kurtosis of wind pressures were computed and stored in the database. Non-

Gaussian time series of wind pressures were numerically simulated for wind load estimates based on FFT technique.

Among the aforementioned publications, only few were given in describing the behavior of coherences of wind pressures. The exponential decaying form proposed by Davenport (1961) was convenient and commonly applied for estimating co-coherences between any two fluctuating wind speeds. Nevertheless, Ogawa et al (1991) and Uematsu et al (2008) adopted another formula, exponential amplitude multiplied by cosine phase, to better approximate co-coherences. Hui et al (2009) modified the exponential decaying form by adding a coefficient to approach the non-unity coherence value at zero frequency for root coherences instead of co-coherences. Lo and Kanda (2012) indicated that a universal form is insufficient to represent all cross spectra, whether in the upstream region or downstream region. Similar qualitative discussion was also given by Sun et al (2011).

In this study, Reynolds number effect and approaching turbulence are taken into consideration for coherence characteristics of wind pressures on dome roofs. To well describe the characteristics of coherences, co-coherences are decomposed to root-coherences and phases. A modified exponential form proposed by Hui et al (2009) is applied in this study for the approximation of root-coherences. In light of the past works on dome issues, it is believed worthy to accumulate more detailed data on aerodynamics of hemispherical domes for proper design purposes of wind loads.

Wind Tunnel Test on Surface Pressure Measurements

All the discussions of coherences are based on wind tunnel tests conducted in a 24.0 m (length) × 4.0 m (width) × 2.6 m (height) boundary layer wind tunnel. Two flows, smooth and turbulent boundary layer flow (hereafter turbulent flow), are simulated. Figure 1 shows the experimental setting for smooth flow simulation. The base plate for installing the dome model is elevated 55.5 cm from the section floor to minimize the boundary layer effect. Except for the turbulence intensity within 4 cm is larger than 5%, the whole profiles remain a small and constant value of 1%~2%. Figure 2 shows the profiles above the base plate to ensure a smooth flow being simulated, where U_δ=6.8 m/sec and 11.8m/sec are selected for two examples under different wind speeds.

Fig. 1 Experimental setting of smooth flow

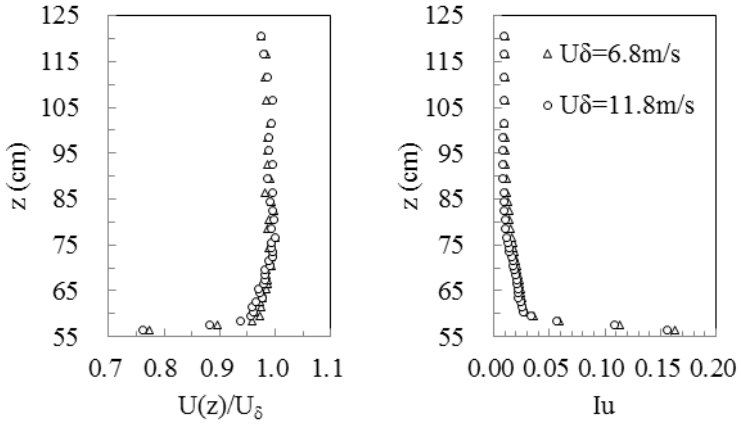

Fig. 2 Mean wind speed profile and turbulence intensity profile of smooth flow

For the turbulent flow, the suburban terrain with power law index α=0.27 is shown in Figure 3. Profiles of mean wind speeds and turbulence intensities are shown in Figure 4 where

the turbulence intensity varies from 25% to 18% at model heights whereas the boundary layer height, δ, is 140 cm and U_δ=9.9 m/sec.

Fig. 3 Experimental setting of turbulence flow

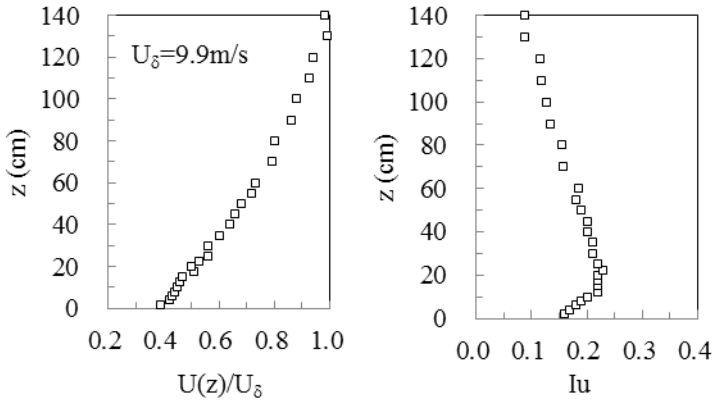

Fig. 4 Mean wind speed profile and turbulence intensity profile of turbulent flow

Three acrylic hemispherical models with diameters of 120 cm, 50 cm, and 20 cm are installed sequentially; the corresponding Reynolds number varies from 6.6×10^4 to 1.9×10^6 by the definition of $Re=U_HD/\upsilon$ where U_H is the mean wind speed at the dome apex, D is the characteristic length of the model, usually the diameter of the hemisphere, and υ is the air density. The blockage percentages of projective areas of domes are calculated to be 5.4%, 0.9%, and 0.15% respectively, which may be considered acceptable for wind tunnel tests.

Pressure taps are arranged along a meridian which is parallel to the approaching wind. The coordinate system of the pressure taps is indicated in Figure 5. Although estimation of design wind loads requires an overall measurement on dome surface, this study intends to focus on those may contain dominant characteristics and simply examines the windward region, the dome apex region, and the wake region. Instantaneous wind pressures are sampled simultaneously by a ZOC pressure scanner system at frequency of 300 Hz. Table 1 shows the basic information of testing models and its corresponding Reynolds numbers. Pressures through the scanner system are then processed by numerical correction of signal distortion based on inverse-FFT techniques.

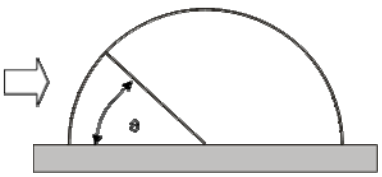

Fig. 5 Coordinate system of pressure taps along the meridian

Table 1: Basic information of dome models

Dome (Diameter in cm)	Reynolds Number	
	Smooth	Turbulent
S (D=20)	6.6×10^4 (SS)	6.7×10^4 (ST)
M (D=50)	4.2×10^5 (MS)	4.3×10^5 (MT)
L (D=120)	1.9×10^6 (LS)	1.8×10^6 (LT)
		(): Case index hereafter

Discussion on Coherence Characteristics of Wind Pressures

In general, design wind loads of a structure can be obtained through the integration of the following equation,

$$S_F(f) = \sum_{i=1}^{m}\sum_{j=1}^{m} X_j X_i A_j A_i S_P(f,i,j) \quad (1)$$

where f is frequency in Hertz; i, j represent two locations of pressures; X_i and X_j are structural mechanical functions at i and j; A_i and A_j are representative areas at i and j; $S_P(f,i,j)$ is the cross spectrum of fluctuating pressures between i and j. Cross spectrum can be related to the following equation where co-coherence function is defined.

$$Coh_{ij}(\Delta s, f) = C_{ij}(\Delta s, f) / \sqrt{S_{Pi}(f) \cdot S_{Pj}(f)} = R_{ij}(\Delta s, f) \cdot e^{\sqrt{-1}\cdot\theta_{ij}(\Delta s, f)} \quad (2)$$

Δs is the net distance between i and j; $C_{ij}(\Delta s, f)$ is the co-spectrum part of $S_P(f,i,j)$. $S_{Pi}(f)$ and $S_{Pj}(f)$ are power spectra of i and j. R_{ij} and θ_{ij} are root-coherence and phase decomposed from co-coherence. Therefore, from Equation (2), to achieve appropriate design wind loads, fine estimation of each component is essential, including the coherence component. For simplicity, θ_{ref} =30°, 90°, and 140° are selected for illustration of coherences in the windward region, the dome apex region , and the wake region. Two parameters are concerned in the following discussions. The first parameter is the location of the reference tap, θ_{ref} , which is in the range of 10°~170°. The second parameter is $\Delta\theta$ ($=|\theta_{ref} - \theta_j|$), the degree difference between the reference tap and the other tap for calculation of coherences.

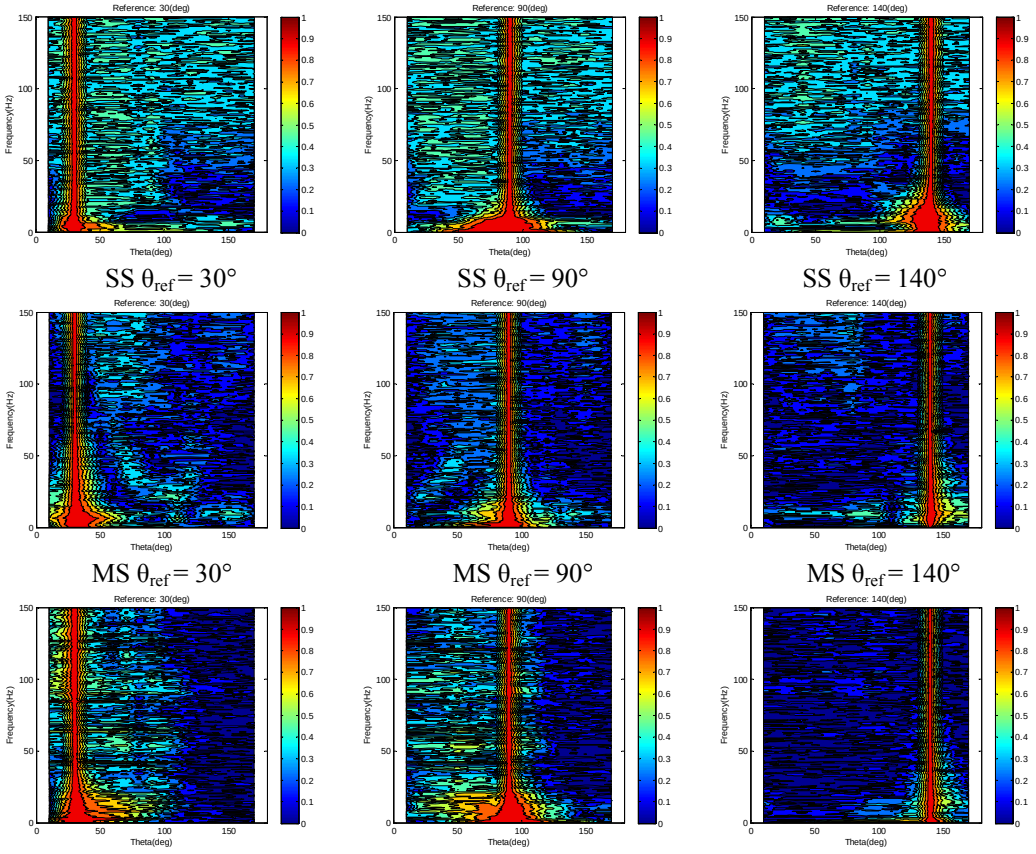

Fig. 6 Root-coherence contours for θ_{ref} = 30°, 90°, and 140° under smooth flow

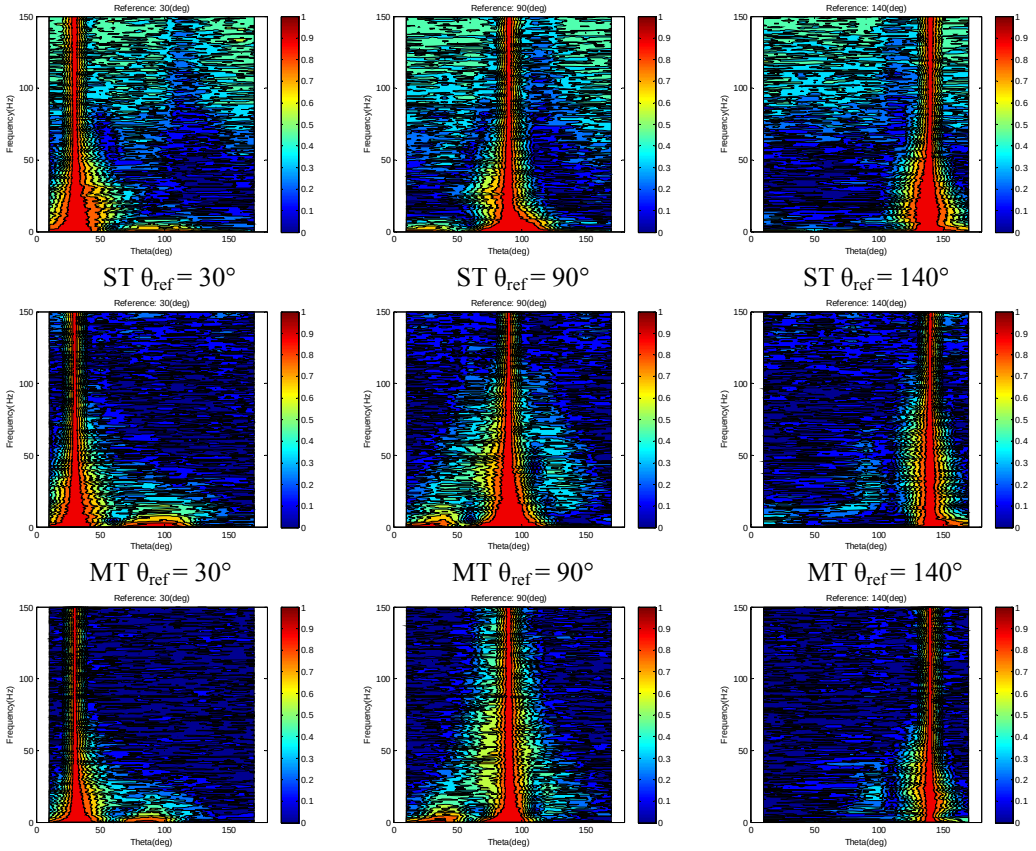

ST θ_{ref} = 30° ST θ_{ref} = 90° ST θ_{ref} = 140°

MT θ_{ref} = 30° MT θ_{ref} = 90° MT θ_{ref} = 140°

LT θ_{ref} = 30° LT θ_{ref} = 90° LT θ_{ref} = 140°

Fig. 7 Root-coherence contours for θ_{ref} = 30°, 90°, and 140° under turbulent flow

Contours in Figure 6 and Figure 7 show the root-coherences in a general view. For the cases in the smooth flow, high coherence value is observed at low frequency range and within the degree difference to the reference tap less than 20°. In the windward region (θ_{ref} =30°), it is clearly indicated that as Reynolds number increases, high coherence extends to a wider frequency range; however, the degree difference between the reference tap and the moving tap is no larger than 10°. The dome apex region (θ_{ref} =90°) and the wake region (θ_{ref} =140°) share a similar pattern as the windward region, except for the lower Reynolds number case. From the three cases, the case SS, whose Reynolds number is in the sub-critical region, shows a contrary pattern from the other two. For the cases in the turbulent flow, the area of high coherence value covers more than that in the smooth flow. Reynolds number is less significant to the contour distributions. Interestingly, in the windward region and the dome apex region, high coherence value is not just indicated near the reference tap, but a small area at lower frequency range with a degree difference of 80°~90° can be observed.

To examine in detail the distribution of root-coherence values over all frequency ranges, Figure 8 shows the cases of $\Delta\theta = \left|\theta_{ref} - \theta_j\right| = 10°$ and $\Delta\theta = 20°$ of Case LT in the windward, dome apex, and wake region. For θ_{ref} =30° in the windward region, the degree difference shows a different coherence value at reduced zero frequency. Larger degree difference lowers the unity at zero frequency. For θ_{ref} =90° in the dome apex region, a dramatic decay of root-coherence value is indicated at low reduced frequency ranges, say 0.0~0.1, due to the degree difference between two taps. It then gradually climbs to 0.5~0.6 at higher reduced frequency ranges, where the decaying distribution is no longer observed. For θ_{ref} =140° in the wake region, the degree difference also result in different trends of

distributions. The decaying phenomenon can be observed in $\Delta\theta = 10°$ in the whole distribution and a clear hump is clearly indicated around reduced frequency 0.1. However, root-coherence value almost remain constant when $\Delta\theta = 20°$. Figure 8 implies that not only the root-coherence value can be non-unity at zero frequency, but also the distribution trend may not be decaying form.

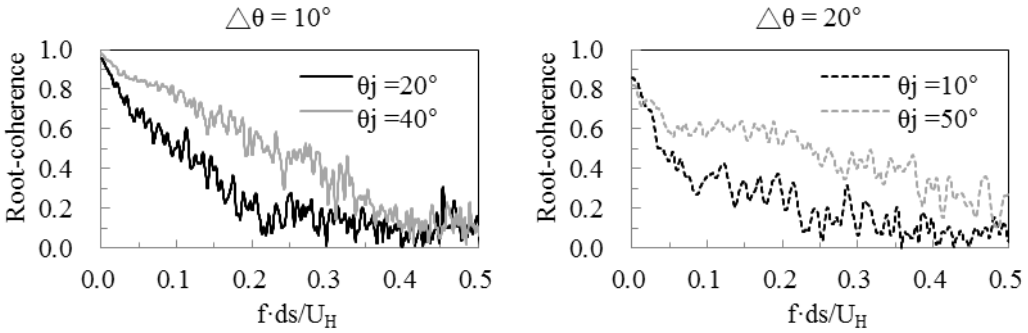

(a) $\theta_{ref} = 30°$

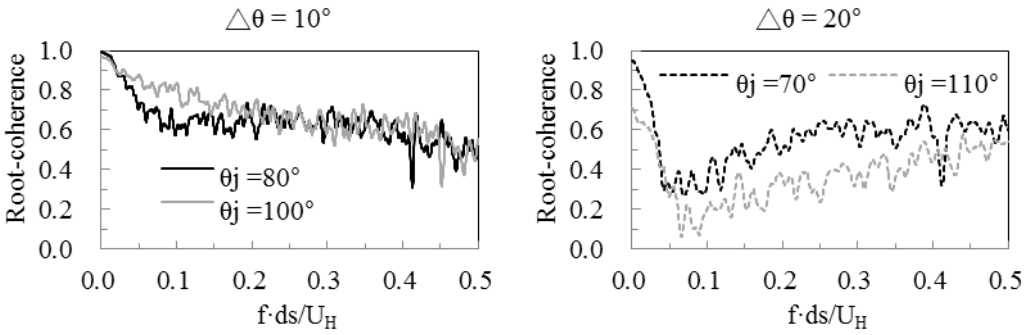

(b) $\theta_{ref} = 90°$

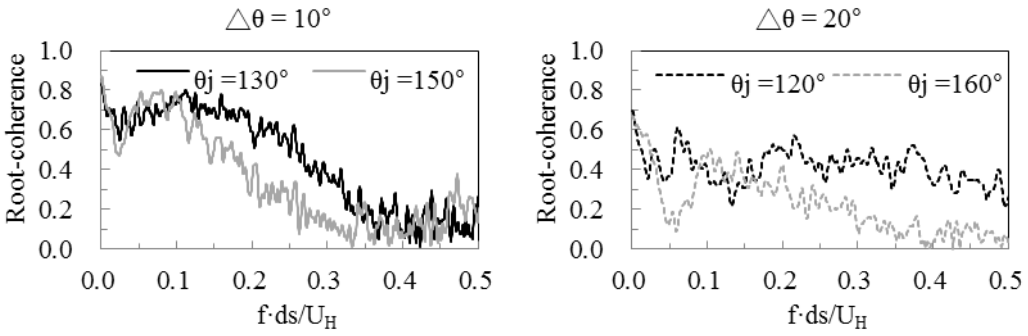

(c) $\theta_{ref} = 140°$

Fig. 8 Root-coherence distributions for $\theta_{ref} = 30°$, 90°, and 140° for Case LT

To properly describe features shown in Figure 8, the exponential decaying form of root-coherence proposed by Davenport (1961) may need further modification, for instance, with some coefficients to fit values at zero frequency. Hui (2009) proposed a simple modified form with two coefficients for approximating root-coherences:

$$R_{ij}(\Delta s, f) = \mathrm{K} \cdot \exp(-C \cdot \frac{f\Delta s}{U_H}) \tag{3}$$

By adding a decaying coefficient, C, the form can approach the decaying trend of the whole distribution; while a modification coefficient, K, can lower the root-coherence value to a non-unity value. Approximation results and fitted coefficients of Case LC are plotted in Figure 9 and 10 for $\Delta\theta = 10°$ and $\Delta\theta = 20°$ respectively. It is easily pointed out from figures that

although the coefficient K describes the non-unity value at zero frequency fairly well, the decaying coefficient C cannot completely define the whole distribution behavior. A further complicated approximation form may be necessary, especially when the separation of flow, reattachment, horse-vortex, or leeward wake occurs and the behavior of wind pressures on the dome surface significantly changes. Figure 11 shows the fitted coefficients along the meridian for the degree difference $\Delta\theta = 10°$ and $\Delta\theta = 20°$. Table 2 lists the fitted coefficients for all cases in the windward region, dome apex, and the wake region.

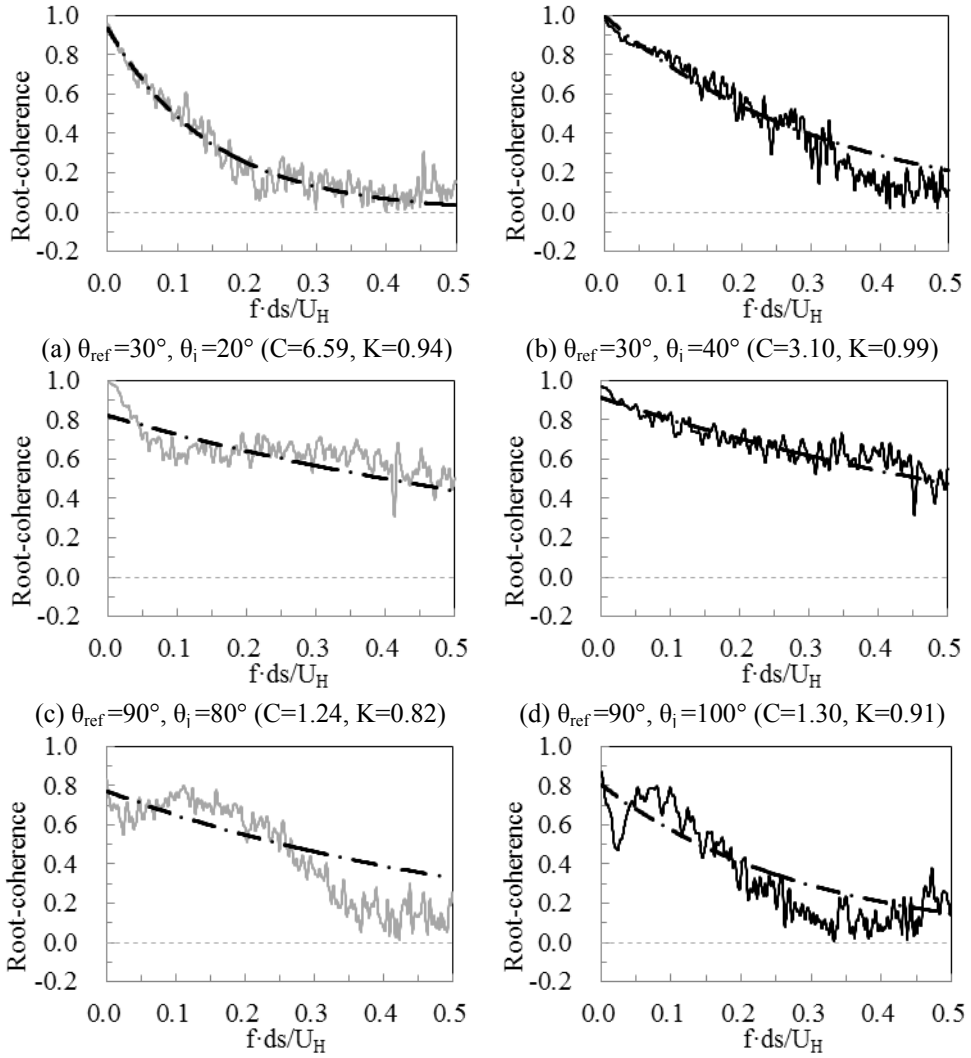

(a) θ_{ref}=30°, θ_i=20° (C=6.59, K=0.94) (b) θ_{ref}=30°, θ_i=40° (C=3.10, K=0.99)

(c) θ_{ref}=90°, θ_i=80° (C=1.24, K=0.82) (d) θ_{ref}=90°, θ_i=100° (C=1.30, K=0.91)

(e) θ_{ref}=140°, θ_j=130° (C=1.70, K=0.77) (f) θ_{ref}=140°, θ_j=150°(C=3.39, K=0.81)

Fig. 9 Fitting results of root-coherences of Case LT for $\Delta\theta$ = 10°

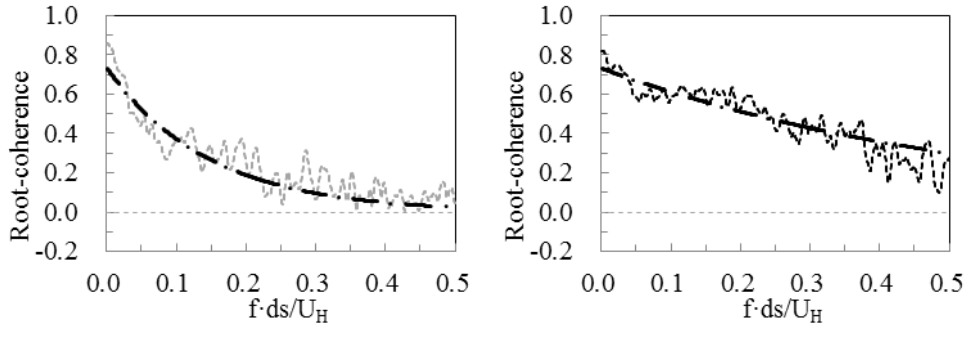

(a) θ_{ref}=30°, θ_j=10° (C=6.81, K=0.74) (b) θ_{ref}=30°, θ_j=50° (C=1.79, K=0.73)

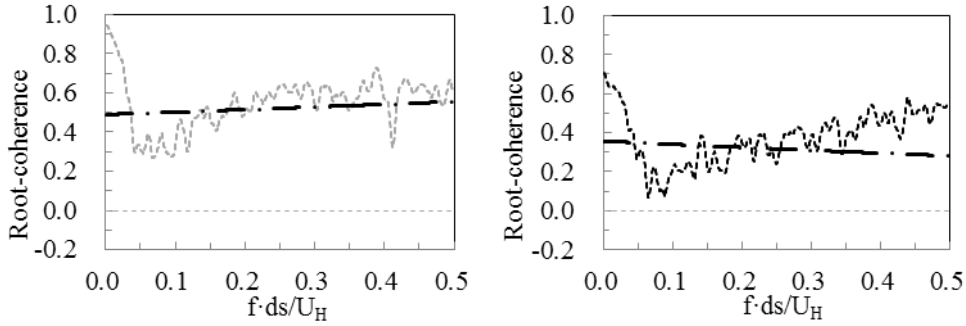

(c) θ_{ref}=90°, θ_i=70° (C=-0.25, K=0.49) (d) θ_{ref}=90°, θ_i=110° (C=0.48, K=0.36)

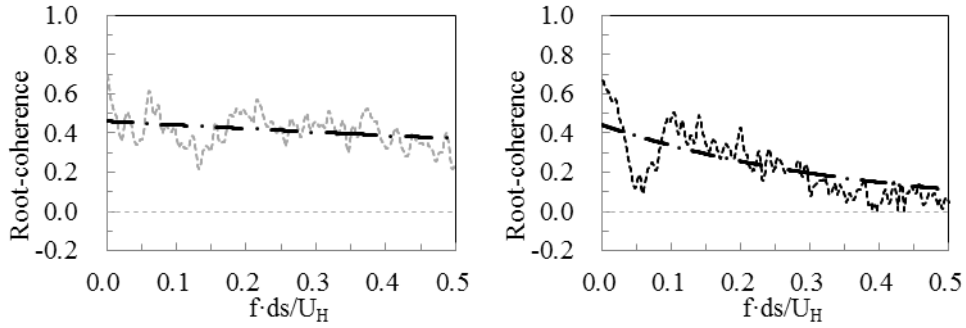

(e) θ_{ref}=140°, θ_j=120° (C=0.43, K=0.46) (f) θ_{ref}=140°, θ_j=160°(C=2.73, K=0.44)

Fig. 10 Fitting results of root-coherences of Case LT for △θ = 20°

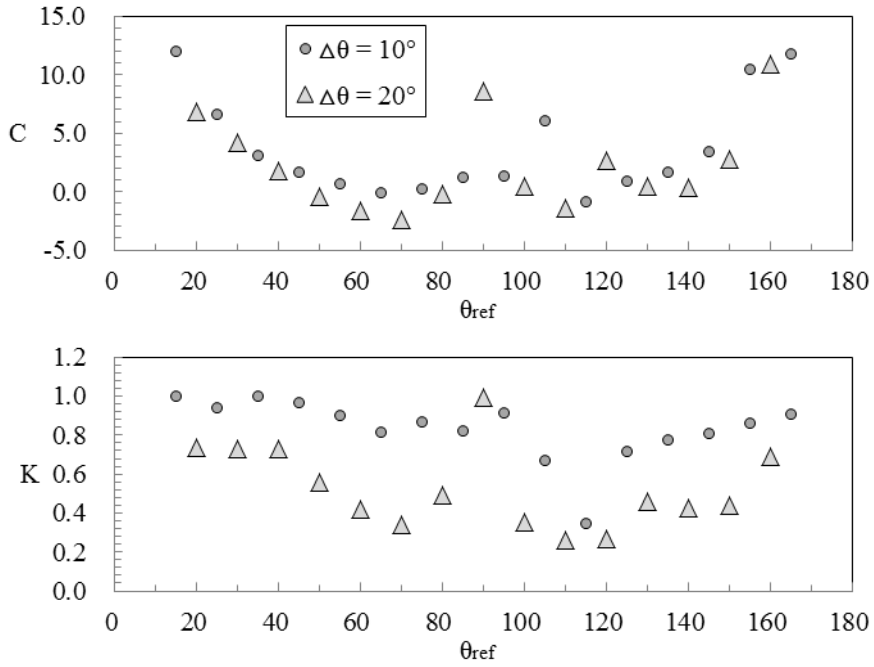

Fig. 11 Fitting coefficients of Equation (3) for Case LT

Conclusions

Root-coherence varies with the location of the reference tap and the degree difference between two taps. Rather than Reynolds number, approaching turbulence introduced by simulated turbulent flow plays a more significant role in defining root-coherences. From analyzed results, a universal root-coherence formula is once again proved insufficient. In general, root-coherences vary significantly at lower frequency ranges, say less than 50Hz, which is within the sensitive range if scaled to a real structural dimension. Contour plots of

root-coherences provide a general qualitative description. Although the modified exponential model proposed by Hui can approach the non-unity value at zero frequency, the decaying form may be the only distribution type for different locations. In order to well estimate design wind loads, an advanced formula for describing cross spectra of fluctuating wind pressures, including the root-coherence and furthermore the phase, should be attempted in the next stage.

Table 2(a) Fitting coefficients C for all cases

	$\Delta\theta = 10°$			$\Delta\theta = 20°$		
θ_{ref} =	30°	90°	140°	30°	90°	140°
SS (Re = 6.6×10^4)	2.65	6.05	8.39	2.78	4.71	5.98
MS (Re = 4.2×10^5)	4.99	5.72	4.40	6.83	4.27	4.19
LS (Re = 1.9×10^6)	3.52	4.50	3.99	3.55	3.80	5.65
ST (Re = 6.7×10^4)	3.01	2.84	3.35	2.41	3.59	2.51
MT (Re = 4.3×10^5)	3.99	2.43	2.06	3.30	2.12	1.64
LT (Re = 1.8×10^6)	4.85	1.27	2.55	4.16	8.55	0.35

Table 2(b) Fitting coefficients K for all cases

	$\Delta\theta = 10°$			$\Delta\theta = 20°$		
θ_{ref} =	30°	90°	140°	30°	90°	140°
SS (Re = 6.6×10^4)	0.71	0.97	1.00	0.63	1.00	0.87
MS (Re = 4.2×10^5)	0.94	0.88	0.63	0.80	0.85	0.61
LS (Re = 1.9×10^6)	0.94	0.99	0.64	0.97	0.95	0.49
ST (Re = 6.7×10^4)	0.98	0.96	0.98	0.79	0.97	0.85
MT (Re = 4.3×10^5)	0.99	0.99	0.86	0.79	0.91	0.62
LT (Re = 1.8×10^6)	0.97	0.87	0.79	0.73	0.99	0.42

References

Cheng, C. M. and Fu, C. L. (2009), Characteristics of Wind Loads on a Hemispherical Dome in Smooth Flow and Turbulent Boundary Layer Flow, Journal of Wind Engineering and Industrial Aerodynamics, 98, 328–344

Davenport, A. G. (1961), Spectrum of Horizontal Gustiness near the Ground in High Winds, Journal of Royal Meteorological Society, 87, 194–211

Lo, Y. L. and Kanda, J. (2012), Cross Spectra of Wind Pressures on Domed Roofs in Boundary Layer Wind Tunnel, Proceedings of the Seventh International Colloquium on Bluff Body Aerodynamics and Applications, Shanghai, China, September 2-6, 2012

Hui, M.C.H., Larsen, A. and Xiang, H.F., (2009), "Wind turbulence characteristics study at the Stonecutters Bridge site : Part II: Wind power spectra, integral length scales and coherences", Journal of Wind Engineering and Industrial Aerodynamics, Vol. 97, pp. 48–59

Ogawa, T., Nakayama, M., Murayama, S., and Sasaki, Y. (1991), Characteristics of Wind Pressures on Basic Structures with Curved Surfaces and Their Response in Turbulent Flow, Journal of Wind Engineering and Industrial Aerodynamics, 38, 427–438

Qiu, Y., Sun, Y., Wu Y., (2011), Power Spectra of Fluctuating Wind Pressures on Spherical Domes, Proceedings of 13th International Conference on Wind Engineering, Amsterdam

Uematsu, Y. and Tsuruishi, R. (2008), Wind Load Evaluation System for the Design of Roof Cladding of Spherical Domes, Journal of Wind Engineering and Industrial Aerodynamics, 96, 2054–2066